LA-UR-85-1315
CONF-8504110--11



Los Alamos National Laboratory is operated by the University of California for the United States Department of Energy under contract W-7405-ENG-36

TITLE: HYBRID TWO-DIMENSIONAL MONTE-CARLO ELECTRON TRANSPORT IN SELF-CONSISTENT ELECTROMAGNETIC FIELDS

LA-UR--85-1315

DE85 010757

AUTHOR(S): R. J. Mason and C. W. Cranfill

SUBMITTED TO: To be presented at the Los Alamos/CEA Joint Conference on Monte-Carlo Methods, Cadarach, France, April 22-26, 1985.

## DISCLAIMER



Los Alamos Los Alamos National Laboratory
Los Alamos, New Mexico 87545

# HYBRID TWO-DIMENSIONAL MONTE-CARLO ELECTRON TRANSPORT IN SELF-CONSISTENT ELECTROMAGNETIC FIELDS

R. J. Mason and C. W. Cranfill

Los Alamos National Laboratory
Los Alamos, New Mexico 87545, USA

## Abstract

The physics and numerics of the hybrid electron transport code ANTHEM are described. The need for the hybrid modeling of laser generated electron transport is outlined, and a general overview of the hybrid implementation in ANTHEM is provided. ANTHEM treats the background ions and electrons in a laser target as coupled fluid components moving relative to a fixed Eulerian mesh. The laser converts cold electrons to an additional hot electron component which evolves on the mesh as either a third coupled fluid or as a set of Monte Carlo PIC particles. The fluids and particles move in two-dimensions through electric and magnetic fields calculated via the Implicit Moment method. The hot electrons are coupled to the background thermal electrons by Coulomb drag, and both the hot and cold electrons undergo Rutherford scattering against the ion background. Subtleties of the implicit E- and B-field solutions, the coupled hydrodynamics, and large time step Monte Carlo particle scattering are discussed. Sample applications are presented.

## I. INTRODUCTION

The modeling of electron transport in laser targets poses a significant challenge to computational theorists. For target design and stability studies the theorist must know where the electron energy goes following deposition. The transport of this energy by electrons is influenced by close collisional scattering in the depths of a target and also by strong electric and magnetic fields in the target interior and corona. The fields are, in part, determined by the target resistivity, which changes as the target is heated by electron deposition. A fully ionized gold foil target, for example, will present more than $10^{24}$ $cm^{-3}$ electrons as background for thermal absorption in the foil interior, while impinging $CO_2$ laser light will be absorbed at coronal points where the electron density is $10^{19}$ $cm^{-3}$. Hot electrons will stream from these nearly collisionless deposition points (the so-called critical surface) through a transition region and into the strongly collisional foil interior. $CO_2$ deposition at $10^{15}$ $W/cm^2$ produces $3 \times 10^{18}$ $cm^{-3}$ densities of 100 keV electrons. At the coronal edge where this hot density is nearly equal to the ion density the cold background electrons are excluded by the hots, so the hot motion constitutes a non-zero net electron current giving rise to B-field. Such self-generated magnetic fields must be expected in all regions bordering moving hot electrons that have appreciably excluded the colds.

While Fokker-Planck modeling[1] has proven useful for the one-dimensional analysis of transport through the transition region between marginal and strongly collsional target regions, its conventional Legendre expanded form fails in the collisionless corona, and its generalization to higher dimensions appears to be impractical.

Conventional Particle-in-cell methods have proven useful in collisionless multidimensional self-consistent problems. However, the collisional extention[2] of PIC methods has until now been limited to weak collisionality, for which the cumulative particle deflections during a calculational time step were restricted to less than $90^{o}$. Furthermore, a pure particle description is generally limited in application to plasmas manifesting only weak density variation, since if ten particles are sufficient to represent the density in a typical region, the minimum resolvable density of neighboring regions must be modeled with one particle unless some complex bookkeeping for particle fission into smaller particles is implemented in the model. In fact, a pure particle description will generally be subject to finite grid instability, which is substantially weaker[3] in implicit models than in explicit ones but still a factor that limits to less than ten the maximum ratio of hot to cold temperatures that can be explored.

On the other hand, a conventional fluid and Ohm's law description of the plasma has the virtue that large density variations present no special difficulties unless the density drops locally so low (as in the corona of a pellet) that the dominance of collisions fails. In target locations where the collisions are strong, the usual fluid assumptions are sufficient to allow for classical hydrodynamics, Joule heating of the electrons as they slip through the ion background, and conventional thermal conduction.

These considerations and these limits of the older, purer models have lead us to the construction of the present hybrid ANTHEM scheme. Earlier one- and two-dimensional efforts[4-6] have contibuted substantially to the present success of the ANTHEM model.

## II. ANTHEM OVERVIEW

### A. Principal Code Features

#### 1. The Fluids

In ANTHEM the ions are a fluid. We assume that their density is everywhere high enough and their temperature low enough so that the inter-ion collision rate justifies the fluid modeling. Similarly, the backgound thermal electrons in a target are modeled as a fluid. We assume that these electrons collide with either the ions in dense regions or with the retaining self-consistent E-fields at the near-vacuum edge of a target, so they acquire at least an isotropic, if not Maxwellian, distribution.

We retain the electron inertial terms in the fluid equations. This eliminates runaway problems in near-collisionless regions and most of the ambiguities of any alternate flux-limited treatment. It has the disadvantage that the overall time step for our calculations is restricted

by a Courant condition set by the fastest electrons, i.e. $\Delta t < \Delta x/v_h$. Usually, the hot electron component will set this time step limit. Use of the fluid background for thermal electrons eliminates the possiblity of finite grid instability heating (a full-particle simulation phenomenon) of the cold backgound electrons. This allows for a nearly arbitrary ratio of hot to cold temperature in our hybrid simulations, e.g. 80 keV hot electrons in a 1 eV background.

In laser problems a part of the deposited energy is generally carried by a separate group of long range suprathermal electrons. In ANTHEM this additional electron component is treated as either a second electron fluid or as a set of collisional PIC particles. As in the case of the thermal electrons, modeling as a fluid is justified by the assumed reflection of the electrons off restraining E-fields. The hot electrons undergo drag against the thermal backgound. In the fluid hot mode the local hot electron density is decreased as the drag proceeds. The drag rate is phenomenologically set at 1/Z times the scattering rate for electrons at an effective temperature set by the local total energy, i.e. at $T_{tot} = T + mu_e^2/3k$, where k is Boltzmann's constant. Both the thermal fluid and the hot fluid are governed by modified Braginskii[7] equations, with the electron moments changed by the gradient of a scalar pressure, by E- and B-fields, and by scattering collisions against the background ions. When the Braginskii scattering rate is large, $\nu_{h,c}\Delta t >> 1$, the hot and cold electron component velocities are driven to the local ion velocity, $u_{h,c} \to u_i$. This behavior is consistent with our use of the component momentum equations

$$\underset{\sim}{j}_\alpha^{(m+1)} = \underset{\sim}{j}_\alpha^{(m)} - \frac{1}{m}[\nabla\cdot\bar{\bar{P}}_\alpha + en_\alpha(E^{(m+1)} + \frac{\underset{\sim}{v}_\alpha}{c} \times \underset{\sim}{B})]\Delta t$$

$$- \nu_\alpha \Delta t(\underset{\sim}{v}_\alpha^{(m+1)} - \underset{\sim}{v}_i^{(m+1)}), \quad \underset{\sim}{j}_\alpha^{(m+1)} = n_\alpha \underset{\sim}{v}_\alpha^{(m+1)} \qquad (1a)$$

for the electrons, $\alpha = h,c$, and

$$\underset{\sim}{j}_i^{(m+1)} = \underset{\sim}{j}_i^{(m)} - \frac{1}{M}[\nabla\cdot\bar{\bar{P}}_i - Zen_i(E^{(m+1)} + \frac{\underset{\sim}{v}_i}{c} \times \underset{\sim}{B})]\Delta t$$

$$+\nu_h \Delta t \frac{n_h}{n_i}(\underset{\sim}{v}_h^{(m+1)} - \underset{\sim}{v}_i^{(m+1)}) + \nu_c \Delta t \frac{n_c}{n_i}(\underset{\sim}{v}_c^{(m+1)} - \underset{\sim}{v}_i^{(m+1)}) \qquad (1b)$$

for the ions. Alternatively, when the details of the evolving hot electron distribution are desired, the hot particle mode is available.

## 2. The Particles

In the hot particle mode two to ten particles are emitted per cell per time step into an emission distribution consistent with experiment or finer scale simulation. To simulate resonance absorption the electrons are ejected as a drifting Maxwellian in a $20^{o}$ cone directed back toward the laser. But for comparison with fluid modeling isotropic Mawellian emission is available in ANTHEM. Also, for various diagnostic tests, such as testing the hot electron range in our treatment of drag, the emission can be set as a monoenergetic beam into or out of the target.

To simulate drag against the thermal background we slow each particle in accordance with the rule $\Delta c/\Delta t = -\text{const.}/c^2$. Here $c^2 = u^2+v^2+w^2$, where u and v are perpendicular to the B-field, and w lies along it. Generally, the drag modeling follows the Ref. 8 procedures. The electrons deposit their energy in the backgound thermal electrons as they are slowed, and should their kinetic energy drop below the local thermal energy, they are absorbed lending their density and total energy to the background. If the hot electron density exceeds the background density, however, no absorption is allowed.

Two alternate schemes are available for the treatment of particle electron scatter. In each case we assume the scatter against ions to be dominant, and approximate the scatter against electrons by increasing the ion collision rate by the factor (1+Z)/Z.

### a. Explicit Scattering

This approach is originally due to Shanny et al.[2]. The electrons are given a deflection through an angle $\theta$ from their original direction, and then the plane of deflection is rotated through a random angle $\phi$ between 0 and $2\pi$. The $\theta$ deflection has a gaussian envelope about a mean Rutherford rate such that the average square deflection is $\langle\theta^2\rangle = \text{const.}/c^3$. The maximum deflection angle is truncated at $90^{o}$. The Braginskii scattering rate relates to the mean scattering angle $\theta$ for hot electrons through the expression $\nu_h\Delta t = \langle\theta^2\rangle/2$. Again, see Ref. 8 for more details. In principal, this explicit scheme is limited to weak scattering conditions, such that $\nu_h\Delta t \ll 1$ and $\theta \ll 1$. This is because following the scatter the electrons are numerically accelerated in the local E- and B-fields and then translated with their new velocities. Thus, consistent with the Courant time step control, the translation can take the fastest electrons across a full cell, i.e. $\Delta\underset{\sim}{r} = \underset{\sim}{v}\Delta t = \Delta x$ or $\Delta y$, where $\underset{\sim}{r}$ and $\underset{\sim}{v}$ are the particle vector position and velocity. However, in strongly collisional regions where $\nu_h\Delta t \gg 1$, the translation should evolve as Brownian motion with the particle excursions reduced to approximately $\Delta\underset{\sim}{r} = c\Delta t/(\nu\Delta t)^{1/2}$. This can be approximated in the explicit model by reducing all excursions through a Brownian flux-limit factor $f_B = 1/[1+(\nu\Delta t)^{1/2}]$ with corresponding $f_B^2$ reductions in the $\underset{\sim}{E}$ and $\underset{\sim}{v} \times \underset{\sim}{B}$ accelerations. However, an implicit scattering treatment should be more exact.

### b. Implicit Scattering

This second procedure is more completely described in the acompanying paper by Cranfill et al.[9] The field accelerations and the scattering accelerations are performed simultaneously. For the two deflection

operations previously described we substitute a rotation operation relative to a randomly oriented collision vector $\underset{\sim}{C}$. Thus, a particle's velocity reorientation in a scattering event becomes much like its redirection on crossing a magnetic field. The particle momentum equation becomes

$$\frac{d\underset{\sim}{v}}{dt} = -\frac{e}{m}(\underset{\sim}{E} + \frac{\underset{\sim}{v} \times \underset{\sim}{B}}{c}) + \underset{\sim}{v} \times \underset{\sim}{C}. \qquad (2)$$

The magnitude of $\underset{\sim}{C}$ is chosen[9] to reproduce the Braginskii Ohm's law scattering rate on the average for a Maxwellian distribution of hot electrons. The particle electrons are advanced with centered velocities. In strong collision regions the effect of the $\underset{\sim}{v} \times \underset{\sim}{C}$ operation is to simply reverse the particle velocities. The mean value of $\underset{\sim}{v}$ over the time step is, therefore, very nearly zero with strong collisions, so the particle excursions with the centered velocity can, indeed, be very small. Detailed analysis[9] shows such excursions to be consistent with Brownian motion.

We note that the drag and scattering effects compete. Once a hot electron has been dragged to background speeds, it is destoyed and scattering ceases. In particular, when $\nu_h \Delta t$ is large, the drag tends also to be strong, especially in low Z materials. In such cases rapid deposition of the hot electrons may render details of the scattering procedure less crucial.

Following the sourcing of particles and the drag calculation, the particle mean density, flux and pressure ($n_h$, $j_h$, and $\bar{P}$) are accumulated for use in the field calculation. At the end of each cycle these moments are again accumulated for diagnostic purposes.

The hot electrons are typically generated at densities of order $3 \times 10^{18}$ $cm^{-3}$ and are significant in the corona and target interior to roughly one tenth this density, so particle fission into smaller units is unnecessary. The steep density rise of the background plasma is readily managed by its contiuous Eulerian fluid treatment.

3. The Fields

ANTHEM calculates the E- and B-fields by the implicit moment method[3,9]. This relieves the restraint of earlier explicit field methods to time steps less than the local plasma period, i.e. $\omega_p \Delta t \gg 1$ is allowed. However, the Courant limit $\Delta t < \Delta x / v_h$ remains. In the moment method Maxwell's equations are solved for a set of advanced sources -- in the present case, predicted current values $j_\alpha^{(m+1)}$. These currents are obtained from Eq. (1) spatially differenced in a simple centered form. Thus, Eq. (1) is combined with

$$\frac{\partial \underset{\sim}{E}}{\partial t} = -4\pi \sum q_\alpha \underset{\sim}{j}_\alpha^{(m+1)} + c\nabla \times \underset{\sim}{B} \qquad (3a)$$

and

$$\frac{\partial \underset{\sim}{B}}{\partial t} = -c\nabla \times \underset{\sim}{E} \qquad (3b)$$

to obtain the future fields. Here $\underset{\sim}{j}_\alpha$ represents the ion and hot and cold electron particle fluxes, for which $q_\alpha = -e$ and $+Ze$. The model is presently restricted to problems manifesting a single $B_z$ component for motion in the x-y plane through $E_x$ and $E_y$ fields.

a. Field Solution Procedure

The fields are determined by first solving Eqs. (1) for $\underset{\sim}{v}_\alpha$ in terms of $\underset{\sim}{E}$. This can be done two ways. For the first (drift) approach the $\underset{\sim}{v} \times \underset{\sim}{B}$ terms are differenced as $\underset{\sim}{v}^{(m+1/2)} \times \underset{\sim}{B}^{(m)}$. For the second (MHD-like) method we use $\underset{\sim}{v}^{(m)} \times \underset{\sim}{B}^{(m+1)}$ or, more simply, $\underset{\sim}{v}^{(m)} \times \underset{\sim}{B}^{(m)}$. The first approach produces factors like $1/[1 + (\omega_c \Delta t)^2]$ in the expressions for $\underset{\sim}{j}_\alpha$, where $\omega_c = eB/mc$. It also produces terms with the dependence $\omega_c(\Delta t)^2/[1 + (\omega_c \Delta t)^2]$. With these, $\partial P/\partial x$ gradients produce y-directed currents, i.e. $\underset{\sim}{E} \times \underset{\sim}{B}$ drift. In the second approach $\underset{\sim}{j}_{\alpha x}$ responds directly only to $\underset{\sim}{E}_x$, and the $\underset{\sim}{v} \times \underset{\sim}{B}$ term acts much like an explicit magnetic pressure. In each case, the $\underset{\sim}{j}_\alpha$ solutions are substituted into Eq. (3a), which is then time integrated and rearranged to give the $E_x$ and $E_y$ components as functions of $\nabla \times B_z$. The resultant $\underset{\sim}{E}$ expressions are then used with Eq. (3b) to provide a single linear elliptic equation for $B_z$.

With the "drift" treatment of $\underset{\sim}{v} \times \underset{\sim}{B}$, the elliptic equation exhibits 9-point coupling of the $B_z$ field to its nearest neighbors, which leads to a 9-diagonal, sparce, non-symmetric matrix that can be solved by either a vectorized ILUCG or a Tchebychev[10] solver. Here, vectorization produces a 5-fold speedup over the corresponding scalar code. Alternatively, the MHD treatment leads to a modified elliptic equation manifesting 5-point coupling. With $\underset{\sim}{v}^{(m)} \times \underset{\sim}{B}^{(m+1)}$ this matrix is non-symmetric and still requires the Tchebychev solver (which demands 27 full mesh arrays). With $\underset{\sim}{v}^{(m)} \times \underset{\sim}{B}^{(m)}$, the matrix for the $B_z$ solve becomes symmetric, and a vectorized ICCG solver[11] is employed (requiring only 13 full mesh arrays). These solvers require typically $3 \times 10^{-2}$ sec for a 50 x 50 mesh on the Los Alamos CRAY XMP, while a full computational cycle takes from 1 to 2 sec, so the field solving is now a negligible part of the ANTHEM calculations. Solutions by the three different $\underset{\sim}{v} \times \underset{\sim}{B}$ linearization methods differ slightly in detail. Presumably the discrepancies could be eliminated by iteration to a $\underset{\sim}{v}^{(m+1/2)} \times \underset{\sim}{B}^{(m+1/2)}$ result. We have thusfar avoided such iterations. In our MHD approach the $\underset{\sim}{v} \times \underset{\sim}{B}$ term corresponds in the standard way to B-field advection at some mean electron velocity, and numerical stablity is assured by our usual Courant limit.

b. The Field Corrections

Without an additional correction these field solutions will fail to preserve quasi-neutrality in steep density gradient regions at, for example, the surface of a target. This is because the predicted $\underline{j}_\alpha$ values, determined from Eqs. (3) once $B_z$ is known, may not agree with the actual currents that lead through the particle and hydrodynamic advancement procedures to new densities $n_\alpha$. In Ref. 3 this defficiency was eliminated in part by correcting the irrotational part of $\underline{E}$ by redetermining $\nabla\cdot\underline{E}$ from $4\pi\sum q_\alpha n_\alpha^{(m)}$ at the end of each cycle. We have found[12] that with density variations exceeding 50 to 1 this procedure is insufficient. Alone, it leads to the erroneous prediciton of electrostatic potential differences exceeding 6 times $kT_h$, when 1 - 2 $kT_h$ is expected.

Two alternate additional corrections have been developed. In the first we correct the rotational part of $\underline{E}$, as well, by adding to $\underline{E}^{(m)}$ a function $\nabla \times \underline{\lambda}$, which is uniquely chosen to leave $\partial B_z/\partial t$ unaltered in Eq. (3b) when the irrotational correction from $\nabla\cdot\underline{E}$ is added. The function $\underline{\lambda}$ obeys an equation very similar to $B_z$ with $\Delta t \to \infty$. It is found with the aid of the Tchebychev solver. More effectively, in the second procedure we carry out a precise bookkeeping of the acutal fluid currents which have flowed during the cycle, and we accumulate the particle currents in a smooth fashion due to Gisler and Jones[13] that is consistent with mass continuity. Any deviation between the actual currents and the predicted currents is then used to provide a field correction $4\pi e\sum q_\alpha \delta\underline{j}_\alpha$ for the next cycle. It can be shown that the longitudinal part of this field correction is equivalent to the Ref. 3 procedure. The additional rotational $\underline{E}$ correction reduces the potential variations across steep gradients to $O(k\bar{T}_h)$ values.

Use of the $\nabla \times \underline{\lambda}$ procedure avoids the need for the modified current accumulation operations which are quite complex. It is, however, somewhat ad hoc, being based on an assumed invariance of the $\underline{B}$ time derivative. In vacua neighboring a target it appears to give slightly more irregular results than the $\delta\underline{j}_\alpha$ procedure. Either of the techniques give substantially more physical results than does use of the irrotational correction alone.

4. Numerical Considerations

Densities, temperatures, and pressures are stored at cell centers in ANTHEM. The currents, velocities and E-fields are stored at cell wall centers. The B-field resides at the cell corners (or nodes). This staggered mesh allows for steep gradients by assuring that $(1/n)\partial P/\partial x$ is not singular, since the n is taken as the average of the densities characterizing P at cell centers (a $10^{-10}$ $cm^{-3}$ density floor saves the P=0 case). This storage also provides a consistent numerical modeling of the $\nabla\cdot$ and $\nabla\times$ operators employed. It does, however, require some complex algebra and averaging[6] to provide both $E_x$ and $E_y$, and $j_{\alpha x}$ and $j_{\alpha y}$ at each cell wall center.

Fully forward time centering has been used for maximum stability in most junctures in the code where it causes no excessive dissipation. With the drift treatment of $\underline{v} \times \underline{B}$ the velocity factor must be centered at half-time, otherwise there can be rapid cooling of the electrons as they spiral in $\underline{B}$. With particle hot electrons, the individual velocities causing translation

must be centered, and the $j_\alpha$ in Eq. (3a) should be centered to preserve the energy of electrons reflected in the sheath. The fluid velocities at the target edge are generally much lower than those of the particles, so such centering in the fluid hot electron mode seems unnecessary.

The fluids are advanced in two phases. In the first "Lagrangian" phase the velocities at the cell boundaries are updated by the action of the pressure gradients, E- and B-fields, and the collisions — the last drives the three velocity fields toward one another. This phase is completed by subsequently moving the cell walls in accordance with their new velocities. In the second "Eulerian" phase the boundaries are moved back to their original locations, while the fluid is advected across the walls into the neighboring cells. Numerical dissipation is minimized during the advection phase by the use of Van Leer corrections, which tune the fluxes at some point between their spatially centered values and their stable donor-cell values such that accuracy is maximized as stability permits. We advect specific entropy in lieu of internal energy to avoid anomalous vacuum edge heating of expanding targets. Reference 8 details these procedures in a one dimensional context.

B. A Typical Cycle

Typcial flow through the code runs as follows. The time step is set based on the various component Courant limits and various maxima and minima, with restrictions on the time step growth per cycle. The critical surface is located for a single laser beam penetrating parallel to the x-axis from the right. Particles are emitted with the selected distribution or hot fluid is created isotropically thus adding to $n_h$ and adjusting $T_h$ at the critical surface. Mean scattering and absorption rates are set for all the cells. The particles are dragged everywhere to lower speed and new moments are accumulated, or the hot electron fluid has its density reduced in accordance with the local absorption rates. The thermal electrons are equilibrated with the ions at the Braginskii rate, and bremsstrahlung energy loss from the thermals is calculated. At this point all the data needed for the implicit field determination is at hand. The $\nabla \cdot \underline{E}$ and $\nabla \times \underset{\sim}{\lambda}$ corrections to the old field are computed, or preferably the $\delta \underset{\sim}{j}_\alpha$ corrections are added. The coefficients to the B-field solver are computed. $B_z$ is determined by one of the fast iterative solvers. $E_x$ and $E_y$ then follow from Eqs. (3a) and (1). Next the hydrodynamics and any particle advancement is completed. First, either the hot particles or the hot fluids are updated. The particles are moved one by one with either the explicit or the implicit advancement scheme. New moments, $n_h$, $\underset{\sim}{j}_h$, etc. are accumulated following the particle repositioning. Then each of the fluids is advanced through the Lagrangian and Advective phases. Finally, we calculate the actual current which flowed and compare it to our current predictions obtained with the field solve. If desired, the field and hydro-particle updates can then be iterated for superior agreement between the predictions and actuality. Joule heating and thermal conduction in the fluid components is then determined. The cycle concludes with periodic print and graphical dumps.

## III. Sample Applications

Sample results from ANTHEM are collected in Figs. 1 through 3. Figures 1 and 2 deal with the largely collisionless response of a low density foil exposed to $10^{14}$ W/cm$^2$ intensity $CO_2$ light. The light arrives from the right and is 35% absorbed. It deposits at the critical, $10^{19}$ cm$^{-3}$ density surface. The spot width is 40 μm, and the full foil width is 200 μm. The foil is initialized with a ramp profile toward the laser that runs from the peak electron density of 2 x$10^{19}$ cm$^{-3}$ down to $10^{17}$ cm$^{-3}$. The foil material is fully ionized hydrogen at a background temperature of 100 eV. Figure 1 frame (a) shows the densities of the ions and the hot electrons after 2.3 ps. The hot electrons have spread toward the vacuum region, where their density is very nearly equal to the ion density. The thermal electrons are largely excluded from this coronal region. The hot electrons have also spread toward the left boundary, where absorbing boundary conditions have been imposed to mock up a much thicker system. Frame (b) shows the temperature of hots colds and ions. Figure 1 is derived for fluid hot electrons. Although the hot electrons are introduced with a 20 keV temperature, they have cooled to near 10 keV, due to their expansion thoughout the foil. The background ions are still at 100 eV. But by some mechanism, possibly Joule heating, the thermal electrons have risen to 1 keV outside the critical surface (this is marked in all the Fig. 1 and 2 frames by a vertical fiducial line). Frame (c) shows the E-field that holds the hot electrons in the foil. The field is zero at the left and right boundaries. The second curve is the electrostatic potential, which rises to roughly 12 keV inside the foil. In the next row frame (d) shows that the B-field has a maximum value of about 0.4 MG in the region of maximum thermal density gradient. Frame (f) shows that the colds are excluded in a cavity in front of the deposition surface. Frame (g) shows the total E-field that must develop to hold the suprathermals in the target and draw thermals into the deposition region. In the final row frame (f) gives a plot of the vector hot electron current field, frame (h) plots the return current vectors, and frame (i), giving the total hot cold and ion current, clearly evidences the circulating pattern that has given rise to $\underline{B}$.

Figure 2 gives additional information about the Fig. 1 foil. Frames (a) through (c) show the hot electron evolution when the suprathermals are treated as particles and the emission is in the form of an isotropic Maxwellian -- to agree most closely with the corresponding fluid hot calculation. Frames (e) through (g) give comparative hot electron contours from multifluid calculation. The qualitative agreement is extemely good. The B-field as calculated from the fluid model is shown in the final row. In each case the hot electrons tend to be trapped on the surface, as first indicated by Forslund and Brackbill[14]. We have found that when the left boundary condition is specular the excluded foil regions [left top and bottom frame (c)] tend to fill from behind, so the surface transport is less pronounced but still in evidence. The right most frames in Fig. 2 are for 4.7 ps, representing about 3 minutes of CRAY XMP time.

Figure 3 collects results for a much denser and larger foil for which the effects of collisions are much more in evidence. The foil is fully ionized gold at 3 kev backgound temperature. It extends 2000 μm across, and the spot size is ten times larger, 400 μm. The suprathermals are emitted at 80

keV in a $20^{o}$ cone towards the laser. Frame (d) shows that the peak Braginskii scattering rate is $\nu\Delta t = 4$. This is active as hot electrons attempt to enter the solid density gold region. Collisions were treated with the implicit model for this run. The explicit collision treatment gave very nearly similar reults, at first to our general disbelief, because the drag rate is so large for these conditions that the particles are usually destroyed upon crossing more than two cells in the dense foil region. Frame (g) shows the u-x phase space for all the hot electrons. Clearly, they are reflected at both the vacuum interface (by E-fields) and at the high density interface (by collisions with the gold ions). Frames (b,c), (e,f) and (h,i) are at approximately equal times and show again that the particle and fluid treatments are in, perhaps surprisingly, good agreement.

## REFERENCES


1. A. R. Bell, R. G. Evans and D. J. Nicholas, Phys. Rev. Lett. 46, 243 (1981).
2. R. Shanny, J. M. Dawson, and J. Greene, Phys. Fluids 10, 1281 (1967).
3. J. U. Brackbill and D. W. Forslund, J. Comp. Phys. 46, 271 (1982).
4. R. J. Mason, J. Comp. Phys. 51, 484 (1983).
5. R. J. Mason, Los Alamos Report LA-1011C (1984).
6. D. Besnard and R. Mason, Limeil Report CEA-N-2413 (1984).
7. S. I. Braginskii, Rev. Plasma Phys. 1, 205 (1965).
8. R. J. Mason, in "Multiple Time Scales", J. Brackbill and B. Cohen, Eds., (Academic Press, 1985). p 233.
   J. Brackbill and B. Cohen, Eds., p. 233.
9. C. Cranfill, J. Brackbill and S. Goldman, in the Proceedings of the Los Alamos/CEA Joint Conference on Monte Carlo Methods, Cadarach, France, April 22-26, 1985.
10. T. Jordan and T. Manteuffel, Los Alamos, prvate communication (1985).
11. T. Jordan, Elliptic Problem Solvers II, (Academic Press,1984), p. 127.
12. R. J. Mason, to be published.
13. G. Gisler and M. Jones, Los Alamos Report LA-UR-85-124 (1985).
14. D. Forslund and J. Brackbill, Phs. Rev. Lett. 48, 1614 (1982).

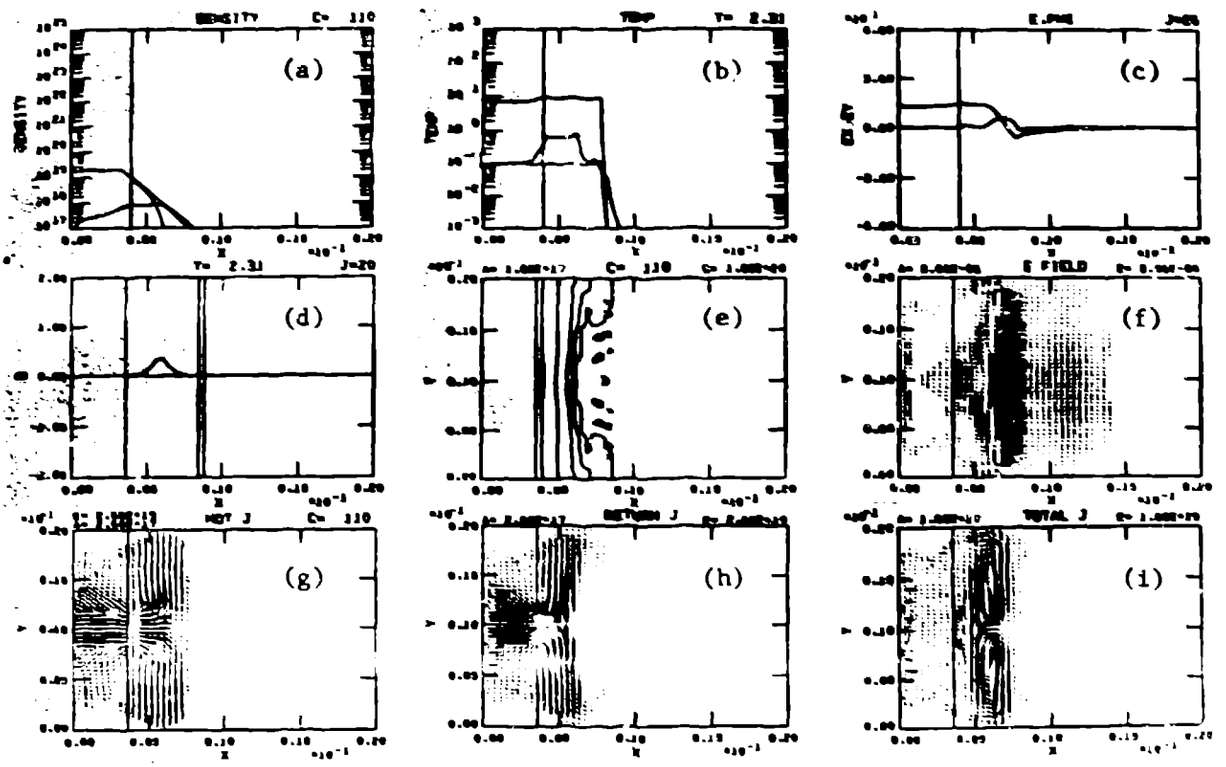


Fig. 1

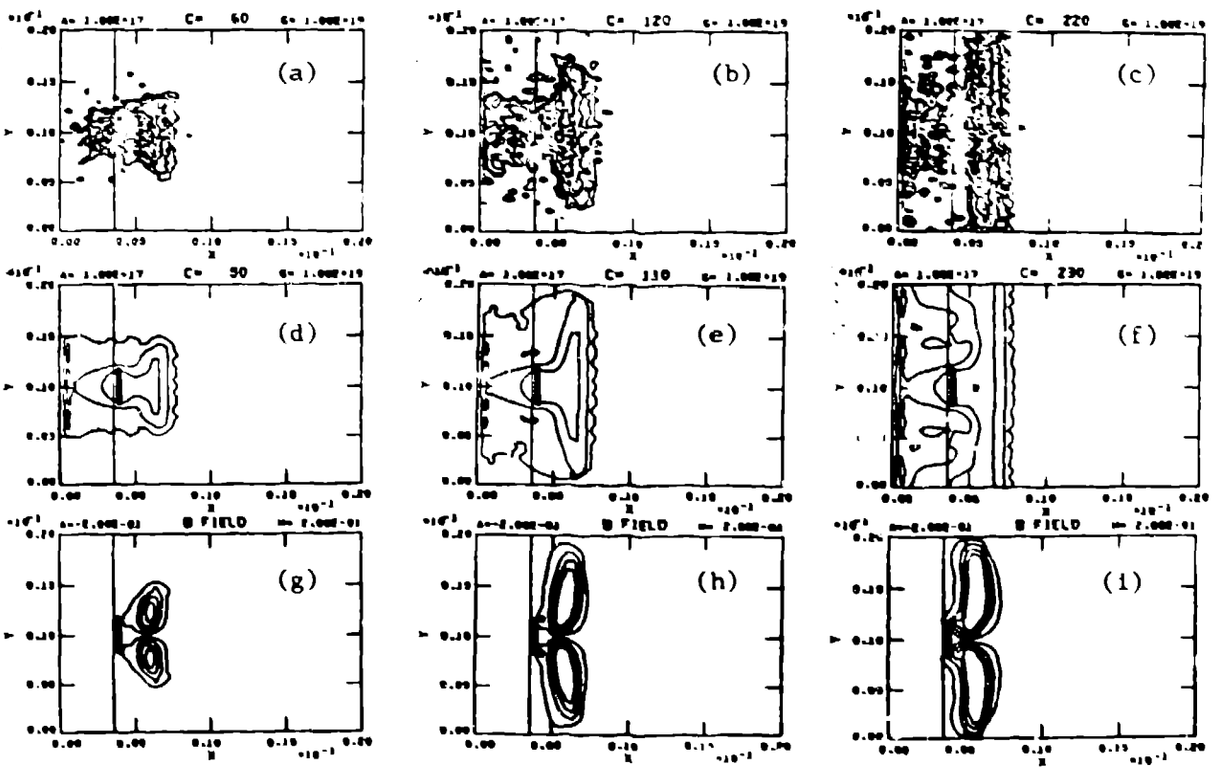


Fig. 2

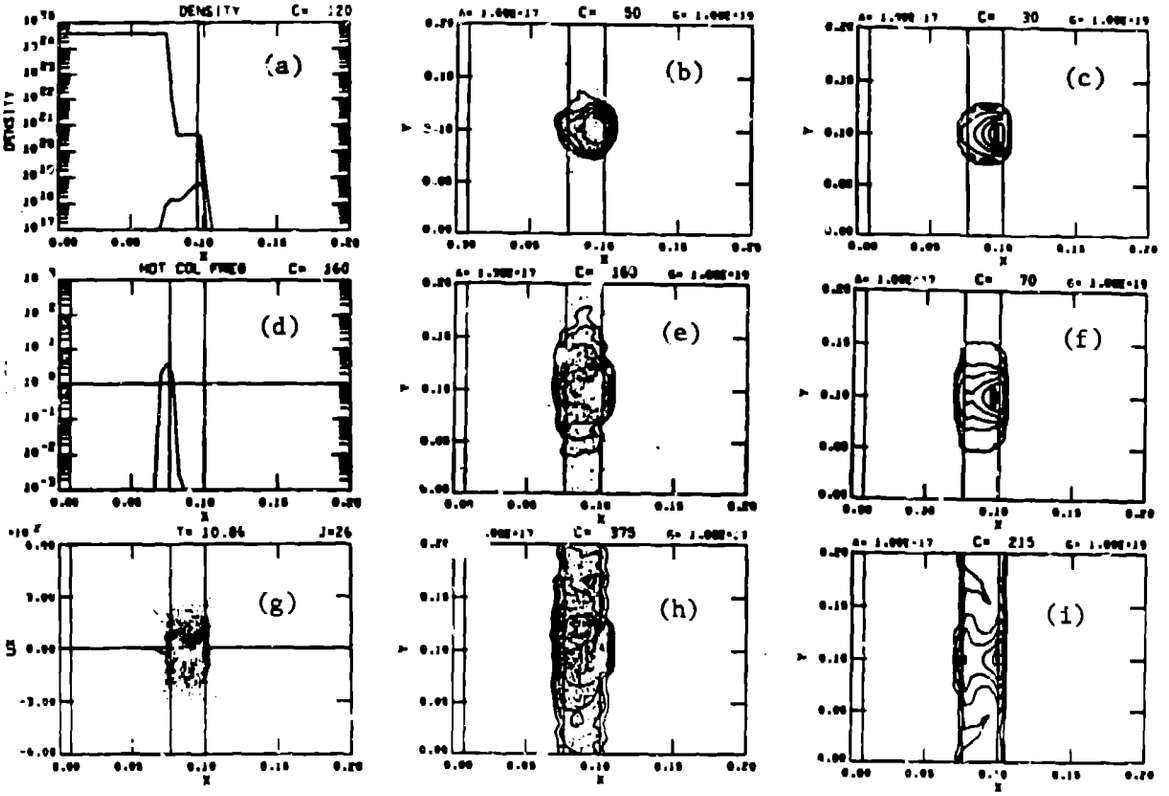


Fig. 3